Synthesis of $Li_2Ni_2(MoO_4)_3$ as a high-performance positive electrode for asymmetric supercapacitors†

Dongwei Du,[a] Rong Lan,[a] Kui Xie,[c] Huanting Wang[b] and Shanwen Tao*[ab]

A NASICON-type compound, $Li_2Ni_2(MoO_4)_3$ was successfully synthesized *via* a combustion method. The as-synthesized $Li_2Ni_2(MoO_4)_3$ is fiber-like grains with an average length of 1–2 μm. As an electrode for pseudocapacitors, in 2 M LiOH, its specific capacitance reached 1137 F g^{-1} and 717 F g^{-1} at current density of 1 A g^{-1} and 20 A g^{-1} respectively, exhibiting 63% capacity retention. Moreover, in asymmetric supercapacitors with an activated carbon electrode as the negative electrode, the energy density of 36.5 W h kg^{-1} was obtained at the average power density of 420 W kg^{-1}. The fabricated asymmetric supercapacitor also exhibited good electrochemical stability, specifically, the specific capacitance was retained at 68% of the initial value even after 10 000 cycles at 2 A g^{-1}. These observations suggest that the prepared $Li_2Ni_2(MoO_4)_3$ is a prospective candidate for high-performance supercapacitors.

1. Introduction

It is believed that there are many issues related to traditional fossil fuel energy supply techniques, such as the climate changes and limited reserves, therefore considerable attention has been paid to renewable energy sources.[1] As a consequence, efficient energy storage systems are in high demand to make the best use of the sources. Electrochemical energy storage systems, including batteries and supercapacitors, are some of the most promising energy storage systems with a broad range of applications. Among different types of electrochemical energy storage devices, supercapacitors have attracted great interest because of their relatively high power density, fast charge/discharge capability and exceptional cycle life.[2–10] Generally, supercapacitors can be classified into two categories depending on the energy storage mechanisms: electrical double layer capacitors (EDLCs) and pseudocapacitors.[11] EDLCs involve reversible adsorption of the ions at the electrode/electrolyte interface without any chemical reactions, which are commonly related to carbon-based materials with high surface area.[12,13] In terms of the pseudocapacitors, fast and reversible faradaic reactions at the electrode surface are utilized to contribute the energy storage capability.[14,15] Typically, the transition metal oxides,[16–18] hydroxides,[19,20] sulfides[21,22] and conducting polymers[23] such as polypyrroles,[24] polyanilines[25] and

polythiophenes[26] are applied as the active materials for pseudo-capacitors. The pseudocapacitors usually present larger specific capacitance than the EDLCs, nevertheless, the lower energy density compared to batteries limit its applications.

As mentioned above, the reversible ion adsorption of the pseudocapacitive materials usually takes place at the electrode surface, which may limit the energy storage capacity. It can be deduced that the energy density could be improved if the bulk ion intercalation is achieved because the extra ion adsorption into the active materials will contribute more capacitance. From this point of view, it is important to explore appropriate materials which can allow the ion intercalation/deintercalation without the structure destruction. Lukatskaya *et al.* demonstrated the electrochemical intercalation of cations including Li^+, Na^+, K^+, NH_4^+, Mg^{2+} and Al^{3+} from aqueous solutions into the two-dimensional Ti_3C_2 MXene layers.[27] Recently, a NASICON-type compound $Li_2Co_2(MoO_4)_3$ was synthesized and its electrochemical performances was investigated in different alkaline electrolyte.[28] It was found that the $Li_2Co_2(MoO_4)_3$ electrode displayed remarkable specific capacitance as pseudocapacitive material for supercapacitors, namely, 1055 to 700 F g^{-1} at the current density from 1 A g^{-1} to 50 A g^{-1} in LiOH solution. Moreover, higher specific capacitance was obtained in lithium-based electrolyte than in sodium and potassium-based electrolytes, which is attributed to the easier intercalation of the small Li^+ ions into the crystallographic structure of the $Li_2Co_2(MoO_4)_3$. As the NASICON-type compounds have a large family, the work opens up a new type of material which could present good supercapacitor performances.

$Li_2Ni_2(MoO_4)_3$, as a member of NASICON-type compounds, has been studied as positive electrode in lithium batteries.[29–31] In this work, the $Li_2Ni_2(MoO_4)_3$ was synthesized *via* a combustion method. Its electrochemical properties were firstly evaluated in

[a] *School of Engineering, University of Warwick, Coventry CV4 7AL, UK. E-mail: S.Tao.1@warwick.ac.uk*

[b] *Department of Chemical Engineering, Monash University, Clayton, Victoria 3800, Australia*

[c] *Key Lab of Design and Assembly of Functional Nanostructure, Fujian Institute of Research on the Structure of Matter, Chinese Academy of Sciences, Fuzhou, Fujian 350002, China*

† Electronic supplementary information (ESI) available: EDS analysis and charge/discharge curves. See DOI: 10.1039/c6ra28580e
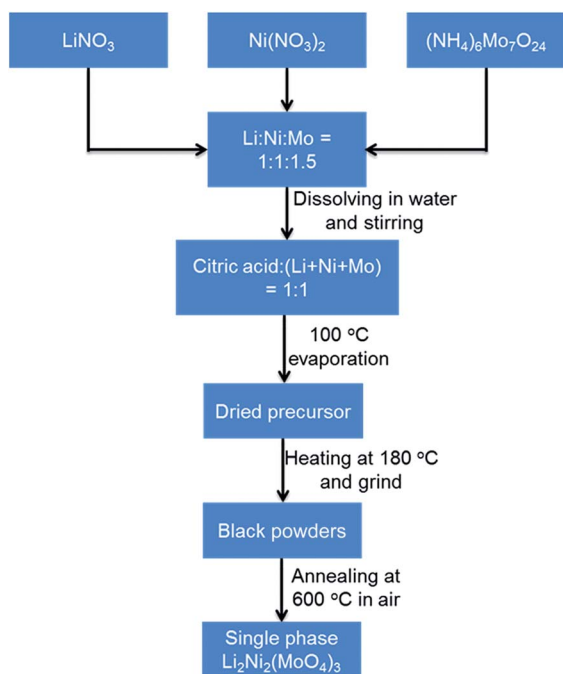
a three-electrode system in alkaline electrolytes. The specific capacitance reaches 1137 F g^{-1} at 1 A g^{-1} and 717 F g^{-1} at 20 A g^{-1} in 2 M LiOH, exhibiting 63% capacity retention. Moreover, the Li$_2$Ni$_2$(MoO$_4$)$_3$ electrode was fabricated with an activated carbon (AC) electrode forming an asymmetric supercapacitor (ASC). The ASC displays an energy density as high as 36.5 W h kg^{-1} at the average power density of 420 W kg^{-1}. It also demonstrates excellent electrochemical stability, specifically, the specific capacitance still retains 68% of the initial value even after 10 000 cycles at 2 A g^{-1}. These results suggest that the prepared Li$_2$Ni$_2$(MoO$_4$)$_3$ is a prospective candidate for the high-performance energy storage devices.

2.   Experimental section

2.1.   Synthesis of Li$_2$Ni$_2$(MoO$_4$)$_3$

The Li$_2$Ni$_2$(MoO$_4$)$_3$ compound was synthesized by a combustion method similar to a method described in previous studies.[29,31] The sequential synthesis procedures are described in Scheme 1. Specifically, aqueous solutions containing the lithium nitrate, nickel nitrate hexahydrate and ammonium molybdate tetrahydrate were homogeneously mixed with an appropriate stoichiometry of Li : Ni : Mo at 1 : 1 : 1.5.

Subsequently, citric acid was added to the solution at stoichiometric amount of 1 : 1 to the total metal ions. The resulted solution was stirred overnight and then heated to boiling at around 100 °C to evaporate water. Then the resulted dried precursor was further heated at 180 °C to obtain black ash. The ash was ground into powders with a mortar. The single-phase powders of Li$_2$Ni$_2$(MoO$_4$)$_3$ in yellow were obtained upon annealing the as-prepared powders at 600 °C for 4 h in ambient air. Na$_2$Ni$_2$(MoO$_4$)$_3$ was synthesized using the same method by replacing LiNO$_3$ with NaNO$_3$.

Scheme 1   Schematic illustration of Li$_2$Ni$_2$(MoO$_4$)$_3$ synthesis process.

2.2.   Electrode preparation for electrochemical characterization

The working electrode was prepared by mixing the as-synthesized Li$_2$Ni$_2$(MoO$_4$)$_3$ powders with acetylene black and polytetrafluoroethylene (PTFE) in a mass ratio of 85 : 10 : 5 in water under magnetic stirring to make slurry. Then the slurry was coated onto a piece of Ni foam (1 × 1 cm^2), pressed at 10 MPa, and finally dried at 60 °C in a vacuum oven overnight. The mass loading of the active materials on the Ni foam was 1.5 mg cm^{-2}.

2.3.   Assemble of Li$_2$Ni$_2$(MoO$_4$)$_3$//AC asymmetric supercapacitor

To fabricate the asymmetric supercapacitor, the as-prepared Li$_2$Ni$_2$(MoO$_4$)$_3$ electrode and an activated carbon (AC) electrode were used as positive electrode and negative electrode, respectively. The AC negative electrode was obtained by mixing the activated carbon (Black Pearl 2000, Cabot) and PTFE at a mass ratio of 95 : 5 in water under constant magnetic stirring. The prepared slurry was spread onto a Ni foam (1 × 1 cm^2) and then pressed at 10 MPa and dried at 60 °C overnight under vacuum. To assemble the full cell, the negative electrode and positive electrode were face to face placed into a container in which the electrolyte was added.[18]

2.4.   Material characterizations

Physical characterization. The thermal analysis was obtained on a NETZSCH 449 F3 thermal analyzer using simultaneous thermogravimetric analysis (TG) and differential scanning calorimetry (DSC). The phase formation of the products was identified by X-ray diffraction (XRD) on a Panalytical X'Pert Pro Multi-Purpose Diffractometer (MPD) with Cu Kalpha1 radiation working at 45 kV and 40 mA. Scanning electron microscopy (SEM) (ZEISS SUPRA 55-VP) was applied to observe the sample morphologies. The elemental compositions were analyzed by energy-dispersive X-ray spectroscopy studies (EDX) attached to the SEM.

Electrochemical measurements. The electrochemical measurements of the as-prepared Li$_2$Ni$_2$(MoO$_4$)$_3$ electrode was performed with a conventional three-electrode cell configuration in different alkaline electrolyte. Besides the Li$_2$Ni$_2$(MoO$_4$)$_3$ working electrode, a piece of Pt mesh (1 × 1 cm^2) and an Ag/AgCl electrode (sat. KCl) were served as counter and reference electrodes, respectively. Cyclic voltammetry (CV), galvanostatic charge–discharge (GCD) and electrochemical impedance spectroscopy (EIS) measurements were carried out on a Solartron 1470E multichannel cell test system. Impedance spectroscopy tests were performed in the frequency range from 100 kHz to 0.01 Hz with a potential amplitude of 5 mV at open circuit potential. The electrochemical performances of the asymmetric supercapacitor were analyzed under a two-electrode mode with Li$_2$Ni$_2$(MoO$_4$)$_3$ as the positive electrode and AC electrode as negative electrode. All the measurements were performed at room temperature in alkaline electrolyte.

2.5. Calculations

The specific capacitance of the electrode in three-electrode mode was calculated from the galvanostatic charge–discharge curves according to the following equation:[32]

$$C_s = \frac{I \times \Delta t}{m_1 \times \Delta V} \tag{1}$$

where C_s is the specific capacitance (F g^{-1}), I is the constant discharge current (A), Δt is the discharge time (s), m_1 is the mass loading of the active materials (g), ΔV is the potential change excluding the IR drop in the discharge step (V). In terms of the two-electrode system, the charge should be balanced between the positive and negative electrodes to obtain high electrochemical performance. The charge stored at the electrode can be calculated by the equation:[33]

$$q = C_s \times \Delta V \times m \tag{2}$$

where C_s is the specific capacitance (F g^{-1}), ΔV is the constant potential range of charge–discharge process (V), m is the mass of the active materials (g). As $q_+ = q_-$, the mass ratio of active material on the positive and negative electrode in a asymmetric supercapacitor can be calculated based on the eqn (2),[34]

$$\frac{m_+}{m_-} = \frac{C_- \times \Delta V_-}{C_+ \times \Delta V_+} \tag{3}$$

Additionally, the specific capacitance of the asymmetric supercapacitor was also calculated from the galvanostatic charge–discharge curves with the same formula:[35]

$$C_s = \frac{I \times \Delta t}{m_2 \times \Delta V} \tag{4}$$

where m_2 is the total mass of the active material in positive and negative electrodes (g).

The energy densities and corresponding power densities of the asymmetric supercapacitor were obtained by the following equations:[35,36]

$$E = \frac{1}{2}C_s V^2 \tag{5}$$

$$P = \frac{E}{\Delta t} \tag{6}$$

where E is the energy density, C_s is the capacitor capacitance, V is the capacitor potential window excluding the IR drop, P is the power density and Δt is the discharge time.[18]

3. Results and discussion

The thermal stability and phase formation process of the Li$_2$Ni$_2$(MoO$_4$)$_3$ was evaluated by simultaneous thermogravimetric analysis (TG) and differential scanning calorimetry (DSC). Fig. 1a shows the typical TG-DSC curves of the Li$_2$Ni$_2$(MoO$_4$)$_3$ precursor complex, the small endothermic peak at ~81 °C is due to desorption of adsorbed water while the exothermic peaks between 200 and 600 °C can be attributed to the decomposition of the precursors. The total weight loss is about 52 wt%, and it
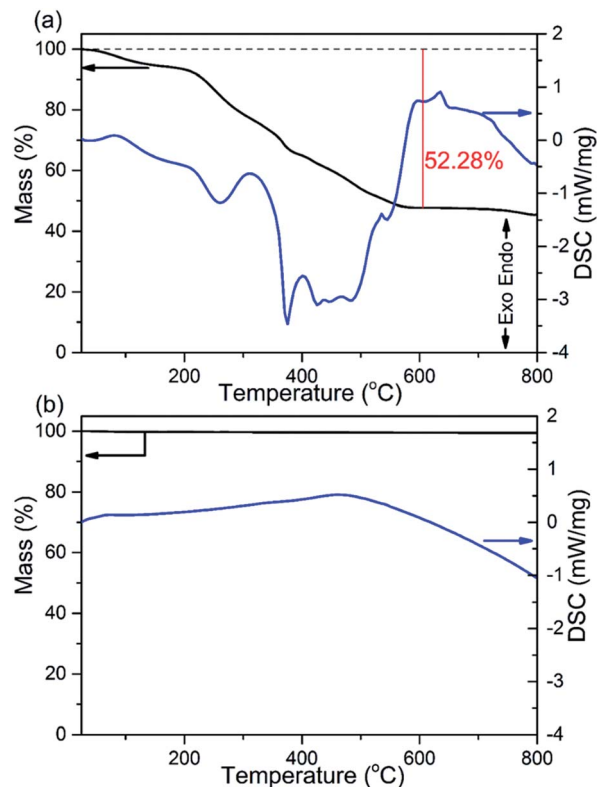

Fig. 1 TG and DSC curves of (a) the Li$_2$Ni$_2$(MoO$_4$)$_3$ precursor complex and (b) the 600 °C annealed Li$_2$Ni$_2$(MoO$_4$)$_3$.

terminates at around 600 °C, indicating the completion of the phase formation reaction. Therefore, the products were annealed at 600 °C and the corresponded TG-DSC curves are in Fig. 1b. The phase purity and structure of the synthesized Li$_2$Ni$_2$(MoO$_4$)$_3$ were examined by X-ray diffraction (XRD). It can be seen from Fig. 2a, the observed peaks of the sample are consistent with the peaks from the orthorhombic Li$_2$Ni$_2$(MoO$_4$)$_3$ (ICCD 04-009-2490), confirming the formation of a well crystalline single-phase with orthorhombic structure. In addition, the polyhedral structure of Li$_2$Ni$_2$(MoO$_4$)$_3$ drawn by CrystalMaker Software is shown in Fig. 2b. The 3D framework is composed of MoO$_4$ tetrahedron and NiO$_6$ octahedron with Li atoms occupying the sites between them. This open structure could favor the intercalation/deintercalation of small-sized ions such as Li$^+$ ions which has been confirmed in previous studies.[29,30] Not only for lithium ion battery, this property can also be used to develop electrode materials for supercapacitors.

The morphology properties of the synthesized Li$_2$Ni$_2$(MoO$_4$)$_3$ were investigated by scanning electron microscopy (SEM). Fig. 3a and b exhibits the SEM images of the sample at different magnifications. It is clear that the sample is composed of fiber-like grains, which is consistent with those in the literatures.[29,31] Fig. 3b indicates the grains are loosely agglomerated which could facilitate electrolyte access during the electrochemical test. In addition, each grain is well connected with the others, which could lead to an improvement on conductivity. The average secondary particle size is roughly 1–2 μm. Energy-

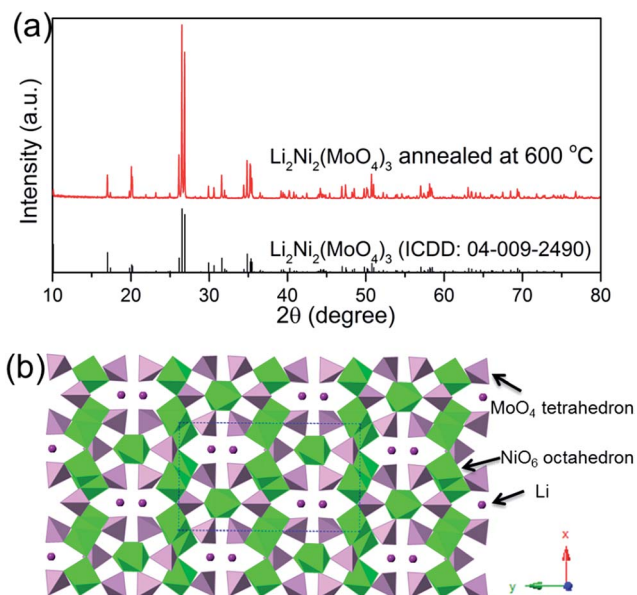**Fig. 2** (a) XRD patterns of the $Li_2Ni_2(MoO_4)_3$ after annealed at 600 °C, (b) crystal structure of $Li_2Ni_2(MoO_4)_3$.

Dispersive X-ray spectroscopy studies (EDX) on selected area indicates the existence of Ni, Mo and O elements (Fig. S1†).

To explore the electrochemical properties of the $Li_2Ni_2(MoO_4)_3$ material, the prepared electrode was tested using a typical three-electrode system. Fig. 4a presents the CV curves of $Li_2Ni_2(MoO_4)_3$ electrode at various scan rate from 1 to 10 mV s^{-1} in the potential range between 0 and 0.5 V vs. Ag/AgCl in 2 M LiOH aqueous solution. The anodic and cathodic peaks indicate the pseudocapacitive behavior of the $Li_2Ni_2(MoO_4)_3$, showing good reversibility. The peak positions are slightly changed with the increase of the scan rate but still reversible. In terms of the CV behaviors in 2 M NaOH solution (Fig. 4c), similar results are obtained. But noticeably, the CV curve in Li-based electrolyte displays larger enclosed area than it in Na-based electrolyte at the same scan rate, implying higher capacitance, which means that the charge delivered by the intercalation/deintercalation of Li$^+$ ions is higher than that of Na$^+$ ions. The possible reason is that, Li$^+$ ions are much smaller than Na$^+$ ions thus would be

easier to be intercalated/deintercalated in the $Li_2Ni_2(MoO_4)_3$ lattice. Fig. 4b shows the GCD curves at various current densities from 1 to 20 A g^{-1} in LiOH. It can be observed that nonlinear charge–discharge profiles are in GCD curves, which further support the pseudocapacitive characteristics of the $Li_2Ni_2(MoO_4)_3$. Fig. 4d compares GCD curves at 1 A g^{-1} in LiOH and NaOH. The specific capacitance of the electrode in LiOH and NaOH calculated from the GCD curves is shown in Fig. 4e. The capacitance decreases from 1137 F g^{-1} (1.7 F cm^{-2}) at 1 A g^{-1} to 717 F g^{-1} (1.08 F cm^{-2}) at 20 A g^{-1}, performing 63% capacity retention. The impact of the ion size is also reflected on the GCD, the capacitances in NaOH are 860 F g^{-1} (1.3 F cm^{-2}) at 1 A g^{-1} and 488 F g^{-1} (0.73 F cm^{-2}) at 20 A g^{-1}, which is much lower than the values obtained in LiOH, which are consistent with the CV results. Overall, it can be concluded that the small size Li$^+$ ions are easier to intercalate into the $Li_2Ni_2(MoO_4)_3$, which also originally contains Li in the structure. To further understand the electrochemical behavior of the $Li_2Ni_2(MoO_4)_3$ electrode, electrochemical impedance spectroscopy (EIS) measurement was performed in the frequency range from 100 kHz to 0.01 Hz at open circuit potential with the amplitude at 5 mV. From Fig. 4f, in both LiOH and NaOH, the Nyquist plots of the $Li_2Ni_2(MoO_4)_3$ electrode are composed of two parts, namely, a semicircle in high-frequency region followed by a linear component in low-frequency region. The intercept of the plots at the real axis represents the equivalent series resistance (R_s), including the ionic resistance of the electrolyte, intrinsic resistance of active materials and the contact resistance between the active materials and current collector,[37–39] the R_s in LiOH is 0.71 Ω while that in NaOH is 0.78 Ω, almost the same, this can be attributed to the tiny ionic resistance difference between LiOH and NaOH. In terms of the semicircle, its diameter represents the charge transfer resistance (R_{ct}) of the system.[37–39] The corresponding R_{ct} values of the $Li_2Ni_2(MoO_4)_3$ electrode are 4.2 Ω and 5.2 Ω in LiOH and NaOH solution respectively, implying the easier and more rapid charge transfer in LiOH solution. In the low-frequency region, the straight line indicates the Warburg impedance (Z_w),[37–39] associating to the diffusion of the electrolyte ions along the bulk $Li_2Ni_2(MoO_4)_3$. The steeper slope of the straight line exhibited in LiOH
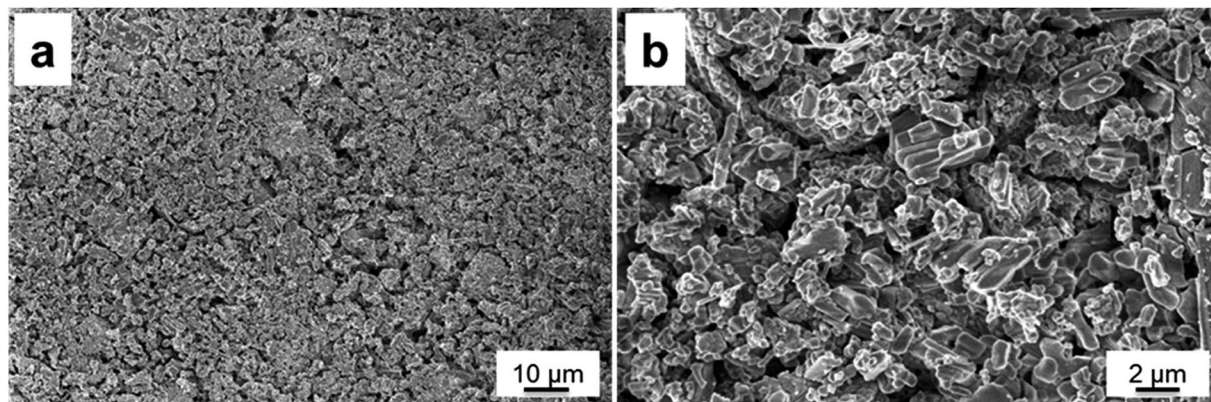

Fig. 3 Typical SEM images of the $Li_2Ni_2(MoO_4)_3$ at (a) low and (b) high magnification.
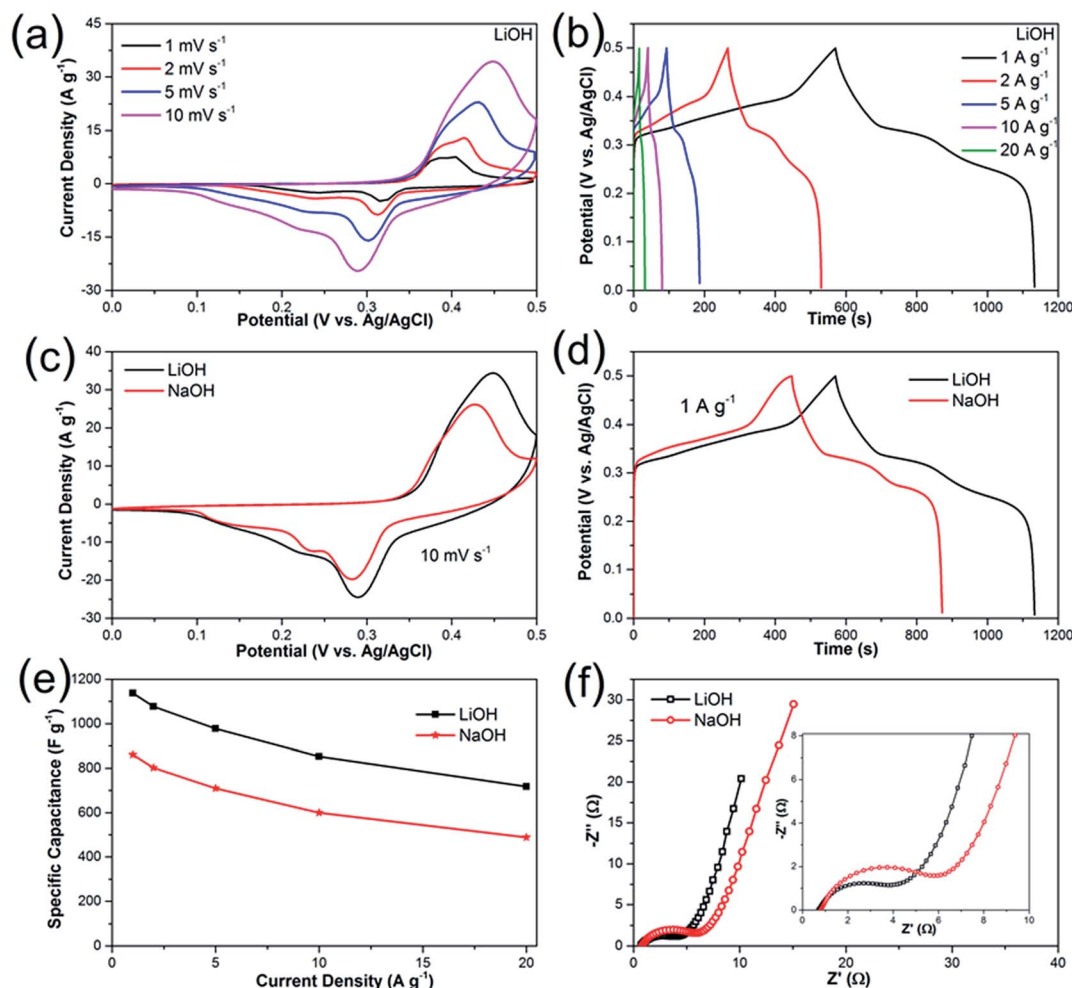
Fig. 4 (a and b) CV curves at different scan rates and GCD curves at various current densities of $Li_2Ni_2(MoO_4)_3$ in 2 M LiOH solution. (c) CV curves at 10 mV s^{-1} in LiOH and NaOH. (d) GCD curves at current density of 1 A g^{-1} in LiOH and NaOH. (e) Specific capacitances at various current densities in LiOH and NaOH. (f) Nyquist plots of $Li_2Ni_2(MoO_4)_3$ electrode carried out at open circuit potential in the frequency range of 100 kHz to 0.01 Hz in LiOH. The inset of (f) shows the impedance in high-frequency region.

demonstrates a smaller Z_w of the LiOH electrolyte ion diffusion, which explains the improved electrochemical performance of the $Li_2Ni_2(MoO_4)_3$ electrode in LiOH.

The high electrochemical performances of $Li_2Ni_2(MoO_4)_3$ electrode such as high capacitance and outstanding rate capability can be attributed to well-connected fiber-like structure, which improves the ion transport. Moreover, the $Li_2Ni_2(MoO_4)_3$, as a NASICON-type material, supplies the channels for the intercalation/deintercalation of Li$^+$ ions without structure destruction.

It is known that the charge stored in the electrode is contributed by diffusion-controlled faradaic process and capacitive process. The specific contribution of diffusion-controlled process and capacitive effects could be quantified by the following equation:[40–43]

$$i = k_1\nu + k_2\nu^{1/2}$$

or

$$i/\nu^{1/2} = k_1\nu^{1/2} + k_2 \qquad (7)$$

where i is the current in CV curves, ν is the scan rate and k_1, k_2 are constants. The terms $k_1\nu$ and $k_2\nu^{1/2}$ represent at a given potential, the current response due to capacitive effects and diffusion-controlled faradaic process, respectively. The k_1 and k_2 can be calculated by plotting $i/\nu^{1/2}$ vs. $\nu^{1/2}$, thus the fraction of the charge from capacitive effects and diffusion-controlled faradaic process could be determined. Fig. 5a demonstrates the diffusion-controlled contribution to the overall charge storage on $Li_2Ni_2(MoO_4)_3$ at scan rate of 5 mV s^{-1} in LiOH electrolyte. 50.7% of the capacitance is contributed by the faradaic process and the remaining portion is from the capacitive effects. Fig. 5b compares the diffusion-controlled process contribution at different scan rates in both LiOH and NaOH. It is clear that the diffusion-controlled process dominates the capacitance at lower scan rate, specifically, around 80% at 1 mV s^{-1} in both LiOH and NaOH. While the capacitive properties increase gradually with the increasing scan rates. It should be noted that at each specific scan rate, the diffusion-controlled contribution in LiOH is higher than that in NaOH, suggesting that the intercalation/deintercalation of the smaller Li$^+$ ions are
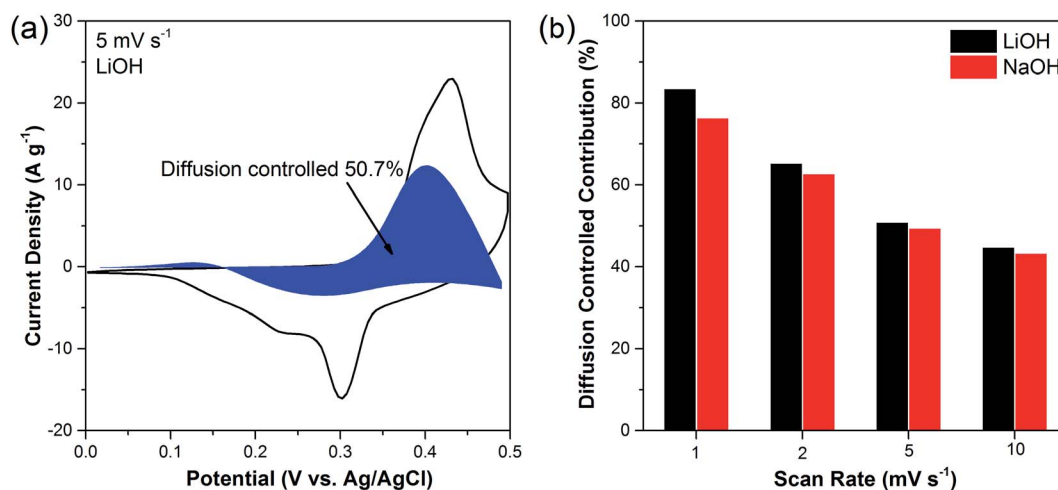
Fig. 5 (a) Capacitive and diffusion-controlled charge storage process at scan rate of 5 mV s^{-1} in LiOH electrolyte, (b) contribution ratio of diffusion-controlled charge storage at various scan rate in LiOH and NaOH electrolyte respectively.

easier than Na^+ ions in the $Li_2Ni_2(MoO_4)_3$, which is in agreement with the CV and GCD results above.

A Na-containing NASICON material with nominal composition $Na_2Ni_2(MoO_4)_3$ was synthesised using the same method to compare the performance with $Li_2Ni_2(MoO_4)_3$. Fig. S2a† shows TG and DSC curves of the $Na_2Ni_2(MoO_4)_3$ precursor complex. Based on the results, the products were annealed at 600 °C and the corresponded X-ray XRD patterns are presented in Fig. S2b.† As no standard data was indexed for the $Na_2Ni_2(MoO_4)_3$ from the database, it is hard to confirm if the single-phase is obtained. Nevertheless, majority of the observed peaks of the sample are consistent with the peaks from $Na_{1.86}Ni_{2.07}(MoO_4)_3$ (ICDD: 00-031-1315) (Fig. S2b†), which may prove that there is a similar structure between the two materials. According to the Na_2MoO_4–$NiMoO_4$–$Fe_2(MoO_4)_3$ phase diagram, the solubility limit of $Na_{2-2x}Ni_{2+x}(MoO_4)_3$ solid solution lies at $0 \leq x \leq 0.7$.[44] Therefore $Na_{1.86}Ni_{2.07}(MoO_4)_3$ ($x = 0.07$) and $Na_2Ni_2(MoO_4)_3$ ($x = 0$) should exhibit the same structure.

The electrochemical properties of nominal $Na_2Ni_2(MoO_4)_3$ in different electrolyte LiOH and NaOH are demonstrated in Fig. S3.† The nominal $Na_2Ni_2(MoO_4)_3$ exhibits higher capacitance in LiOH than in NaOH, implying the charge delivered by the intercalation/deintercalation of Li^+ ions is higher than that of Na^+ ions. It can deduce that in the $Na_2Ni_2(MoO_4)_3$ lattice, Li^+ ions are easier to be intercalated/deintercalated than Na^+ ions, which could be attributed to the smaller size of Li^+ ions. The highest capacitance of nominal $Na_2Ni_2(MoO_4)_3$ performed is 835 F g^{-1} at 1 A g^{-1} in LiOH, which is still lower than the value obtained by $Li_2Ni_2(MoO_4)_3$ (1137 F g^{-1}). The $Na_2Ni_2(MoO_4)_3$ also shows a larger resistance than $Li_2Ni_2(MoO_4)_3$ (Fig. S3d†). Similar to the $Li_2Ni_2(MoO_4)_3$, the capacitance contribution of diffusion-controlled process is larger in LiOH at a given scan rate, while the percentage decreases gradually with the increase of the scan rate in both LiOH and NaOH (Fig. S4†). In conclusion, the overall performance of $Li_2Ni_2(MoO_4)_3$ is better than $Na_2Ni_2(MoO_4)_3$.

To further investigate the electrochemical performances of $Li_2Ni_2(MoO_4)_3$ under practical conditions, we have assembled

an asymmetric supercapacitor (ASC) by employing the prepared $Li_2Ni_2(MoO_4)_3$ electrode as positive electrode and AC electrode as negative electrode. The electrochemical properties of AC electrode exhibits typical features of double layer capacitors (see more details in Fig. S5†). A series of CV measurements at different voltage windows were performed at 5 mV s^{-1} to determine the optimal working potential of the ASC. According to the Fig. 6a, the stable operating voltage window can be extended as high as 1.7 V, and the polarization curve becomes very obvious when the potential increases to 1.8 V, indicating severe electrolysis of water. Therefore, all the measurements of the ASC were carried out between 0 and 1.7 V. Fig. 6b depicts the CV behaviors of the ASC at different scan rates ranging from 1 to 20 mV s^{-1}. It should be noticed that the ASC performs quasi-rectangular CV curves in all scans, illustrating that the capacitance is contributed by both electric double-layer capacitance and pseudocapacitance. The charge–discharge curves measured at the current densities from 0.5 to 20 A g^{-1} are shown in Fig. 6c. The discharge curves are nonlinear especially at lower current densities, suggesting combination effects of the electric double-layer capacitance and pseudocapacitance for the ASC, which coincides with the above CV results. The specific capacitance calculated from the GCD curves is presented in Fig. 6d. The capacitance is 93 F g^{-1} at current densities of 0.5 A g^{-1}, and the value gradually deceases to 73 F g^{-1} at 2 A g^{-1}, which is comparable with some previous ASCs.[45,46] Impressively, the as-fabricated asymmetric supercapacitor reveals excellent rate capability from 5 to 20 A g^{-1}: the capacitances are 67, 64, 62 and 59 F g^{-1} at current densities of 5, 10, 15 and 20 A g^{-1}, respectively. To further investigate the durability of the asymmetric supercapacitor, the cycling performance was evaluated at 2 A g^{-1} (Fig. 6e). The specific capacitance decreases about 20% of the initial value for the first 2000 cycles, which might be caused by the dissolution of the active materials[47] and the destruction of the electrode under rapid redox reactions.[48] The electrode experiences a decrease around 10% of the capacitance during the rest 8000 cycles, demonstrating excellent electrochemical
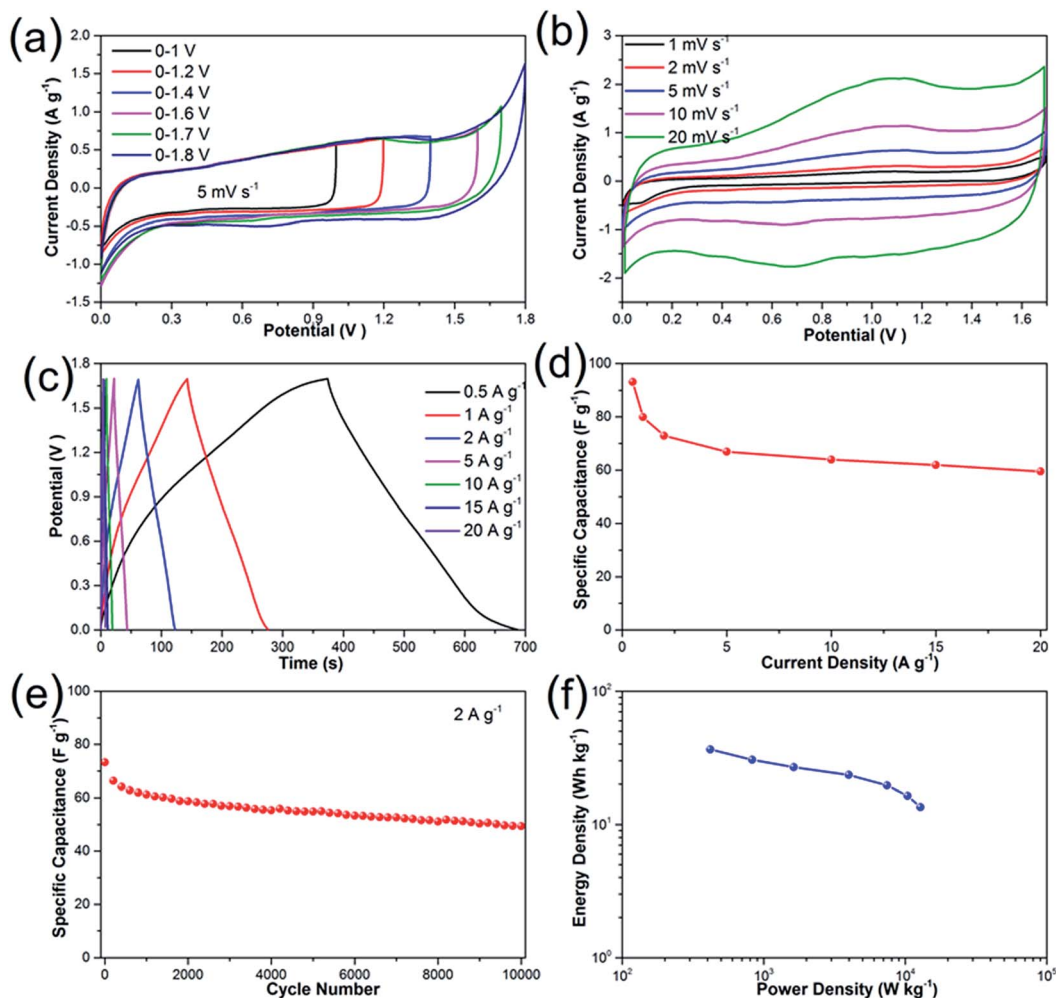
Fig. 6 Electrochemical properties of $Li_2Ni_2(MoO_4)_3$//AC asymmetric supercapacitor: (a) CV curves at various voltage windows at 5 mV s^{-1}; (b) CV curves with a voltage window of 0–1.7 V at various scan rate; (c) galvanostatic charge–discharge curves at various current densities; (d) specific capacitance at various current densities. (e) Cycling performances of the asymmetric supercapacitor for 10 000 cycles at 2 A g^{-1}; (f) Ragone plots of the supercapacitor.

stability. The overall specific capacitance retention is 68% after 10 000 cycles, which can be also evidenced by first and last ten charge–discharge curves (Fig. S6†). The performance decay could be caused by the irreversibility of the Faraday reaction or the destruction of active materials after numerous redox reactions.[7,49] The Ragone-plots of the asymmetric supercapacitor depending on the discharge curved are displayed in Fig. 6f. A maximum energy density of 36.5 W h kg^{-1} is delivered at the power density of 420 W kg^{-1} based on the total mass. It maintains 13.5 W h kg^{-1} at high power density of 12 783 W kg^{-1}.

4.   Conclusions

In summary, we have successfully synthesized the $Li_2Ni_2(MoO_4)_3$ through a combustion method. The $Li_2Ni_2(MoO_4)_3$ electrode exhibits excellent electrochemical performances and it displays higher specific capacitance in LiOH than in NaOH, which can be attributed to the easier intercalation/deintercalation of small Li$^+$ ions in the NASICON-type structure. The specific capacitance reaches 1137 F g^{-1} at 1 A g^{-1} in 2 M LiOH, and still maintains

63% at 20 A g^{-1}. Moreover, in an asymmetric supercapacitor (ASC) with an activated carbon electrode as negative electrode, it delivers energy density as high as 36.5 W h kg^{-1} at the average power density of 420 W kg^{-1}. After 10 000 cycles at 2 A g^{-1}, the capacitance retains 68% of the initial value, showing reasonably good stability. The remarkable specific capacitance with reasonable cycling stability suggest the potential of the $Li_2Ni_2(MoO_4)_3$ to be used as a high-performance candidate for energy storage.

Acknowledgements

References

1 L. L. Zhang and X. Zhao, *Chem. Soc. Rev.*, 2009, **38**, 2520–2531.

2 Y. Zhu, S. Murali, M. D. Stoller, K. Ganesh, W. Cai, P. J. Ferreira, A. Pirkle, R. M. Wallace, K. A. Cychosz and M. Thommes, *Science*, 2011, **332**, 1537–1541.

3 P. Simon and Y. Gogotsi, *Nat. Mater.*, 2008, **7**, 845–854.

4 S. Chen, W. Xing, J. Duan, X. Hu and S. Z. Qiao, *J. Mater. Chem. A*, 2013, **1**, 2941–2954.

5 X. H. Xiong, D. Ding, D. C. Chen, G. Waller, Y. F. Bu, Z. X. Wang and M. L. Liu, *Nano Energy*, 2015, **11**, 154–161.

6 L. Zhu, Y. Liu, C. Su, W. Zhou, M. L. Liu and Z. P. Shao, *Angew. Chem., Int. Ed.*, 2016, **55**, 9575–9578.

7 Y. Zhao, L. Hu, S. Zhao and L. Wu, *Adv. Funct. Mater.*, 2016, **26**, 4085–4093.

8 Q. Zhang, C. Liao, T. Zhai and H. Li, *Electrochim. Acta*, 2016, **196**, 470–478.

9 N. Wang, P. Zhao, K. Liang, M. Q. Yao, Y. Yang and W. C. Hu, *Chem. Eng. J.*, 2017, **307**, 105–112.

10 P. Zhang, J. Y. Zhou, W. J. Chen, Y. Y. Zhao, X. M. Mu, Z. X. Zhang, X. J. Pan and E. Q. Xie, *Chem. Eng. J.*, 2017, **307**, 687–695.

11 G. Yu, X. Xie, L. Pan, Z. Bao and Y. Cui, *Nano Energy*, 2013, **2**, 213–234.

12 T. Lin, I.-W. Chen, F. Liu, C. Yang, H. Bi, F. Xu and F. Huang, *Science*, 2015, **350**, 1508–1513.

13 M. D. Stoller, S. Park, Y. Zhu, J. An and R. S. Ruoff, *Nano Lett.*, 2008, **8**, 3498–3502.

14 C. Xiang, M. Li, M. Zhi, A. Manivannan and N. Wu, *J. Power Sources*, 2013, **226**, 65–70.

15 H. Lai, Q. Wu, J. Zhao, L. Shang, H. Li, R. Che, Z. Lyu, J. Xiong, L. Yang and X. Wang, *Energy Environ. Sci.*, 2016, **9**, 2053–2060.

16 G. Xiong, K. Hembram, R. Reifenberger and T. S. Fisher, *J. Power Sources*, 2013, **227**, 254–259.

17 X. Yu, B. Lu and Z. Xu, *Adv. Mater.*, 2014, **26**, 1044–1051.

18 D. D. Du, R. Lan, W. Xu, R. Beanland, H. T. Wang and S. W. Tao, *J. Mater. Chem. A*, 2016, **4**, 17749–17756.

19 Y.-Z. Su, K. Xiao, N. Li, Z.-Q. Liu and S.-Z. Qiao, *J. Mater. Chem. A*, 2014, **2**, 13845–13853.

20 J. Ji, L. L. Zhang, H. Ji, Y. Li, X. Zhao, X. Bai, X. Fan, F. Zhang and R. S. Ruoff, *ACS Nano*, 2013, **7**, 6237–6243.

21 H. Chen, J. Jiang, L. Zhang, D. Xia, Y. Zhao, D. Guo, T. Qi and H. Wan, *J. Power Sources*, 2014, **254**, 249–257.

22 M. Acerce, D. Voiry and M. Chhowalla, *Nat. Nanotechnol.*, 2015, **10**, 313–318.

23 G. A. Snook, P. Kao and A. S. Best, *J. Power Sources*, 2011, **196**, 1–12.

24 L.-Z. Fan and J. Maier, *Electrochem. Commun.*, 2006, **8**, 937–940.

25 Y. Meng, K. Wang, Y. Zhang and Z. Wei, *Adv. Mater.*, 2013, **25**, 6985–6990.

26 R. B. Ambade, S. B. Ambade, N. K. Shrestha, Y.-C. Nah, S.-H. Han, W. Lee and S.-H. Lee, *Chem. Commun.*, 2013, **49**, 2308–2310.

27 M. R. Lukatskaya, O. Mashtalir, C. E. Ren, Y. Dall'Agnese, P. Rozier, P. L. Taberna, M. Naguib, P. Simon, M. W. Barsoum and Y. Gogotsi, *Science*, 2013, **341**, 1502–1505.

28 K. M. Hercule, Q. Wei, O. K. Asare, L. Qu, A. M. Khan, M. Yan, C. Du, W. Chen and L. Mai, *Adv. Energy Mater.*, 2015, **5**, DOI: 10.1002/aenm.201500060.

29 S. Prabaharan, A. Fauzi, M. Michael and K. Begam, *Solid State Ionics*, 2004, **171**, 157–165.

30 K. Begam and S. Prabaharan, *J. Power Sources*, 2006, **159**, 319–322.

31 K. Begam, M. Michael, Y. Taufiq-Yap and S. Prabaharan, *Electrochem. Solid-State Lett.*, 2004, **7**, A242–A246.

32 J. Yang, X. Duan, W. Guo, D. Li, H. Zhang and W. Zheng, *Nano Energy*, 2014, **5**, 74–81.

33 Z. Fan, J. Yan, T. Wei, L. Zhi, G. Ning, T. Li and F. Wei, *Adv. Funct. Mater.*, 2011, **21**, 2366–2375.

34 V. Khomenko, E. Raymundo-Pinero and F. Béguin, *J. Power Sources*, 2006, **153**, 183–190.

35 X. Wang, A. Sumboja, M. Lin, J. Yan and P. S. Lee, *Nanoscale*, 2012, **4**, 7266–7272.

36 S. Peng, L. Li, H. B. Wu, S. Madhavi and X. W. D. Lou, *Adv. Energy Mater.*, 2015, **5**, 1401172.

37 X. Zhang, Y. Zhao and C. Xu, *Nanoscale*, 2014, **6**, 3638–3646.

38 S. E. Moosavifard, J. Shamsi, S. Fani and S. Kadkhodazade, *RSC Adv.*, 2014, **4**, 52555–52561.

39 M.-C. Liu, L. Kang, L.-B. Kong, C. Lu, X.-J. Ma, X.-M. Li and Y.-C. Luo, *RSC Adv.*, 2013, **3**, 6472–6478.

40 T. Brezesinski, J. Wang, S. H. Tolbert and B. Dunn, *Nat. Mater.*, 2010, **9**, 146–151.

41 M. S. Javed, X. Han, C. Hu, M. Zhou, Z. Huang, X. Tang and X. Gu, *ACS Appl. Mater. Interfaces*, 2016, **8**, 24621–24628.

42 X. Shan, D. S. Charles, Y. Lei, R. Qiao, G. Wang, W. Yang, M. Feygenson, D. Su and X. Teng, *Nat. Commun.*, 2016, **7**, 13370.

43 X. Xia, D. Chao, Y. Zhang, J. Zhan, Y. Zhong, X. Wang, Y. Wang, Z. X. Shen, J. Tu and H. J. Fan, *Small*, 2016, **12**, 3048–3058.

44 N. M. Kozhevnikova and A. V. Imekhenova, *Russ. J. Inorg. Chem.*, 2009, **54**, 638–643.

45 Y. Xu, J. Wei, L. Tan, J. Yu and Y. Chen, *J. Mater. Chem. A*, 2015, **3**, 7121–7131.

46 S. H. Kazemi, M. Tabibpour, M. A. Kiani and H. Kazemi, *RSC Adv.*, 2016, **6**, 71156–71164.

47 Y. Li, J. Jian, Y. Fan, H. Wang, L. Yu, G. Cheng, J. Zhou and M. Sun, *RSC Adv.*, 2016, **6**, 69627–69633.

48 Y. Zhao, L. Hu, S. Zhao and L. Wu, *Adv. Funct. Mater.*, 2016, **26**, 4085–4093.

49 Y. Li, J. Jian, L. Xiao, H. Wang, L. Yu, G. Cheng, J. Zhou and M. Sun, *Mater. Lett.*, 2016, **184**, 21–24.